




# Preparation and characterization of hematite nanoparticles-decorated zinc oxide particles (ZnO/Fe<sub>2</sub>O<sub>3</sub>) as photoelectrodes for solar cell applications

Letícia G. da Trindade<sup>1</sup> , Gabriel Yuji Hata<sup>2</sup>, Josiane Carneiro Souza<sup>3</sup>, Mario R. S. Soares<sup>3</sup>, Edson Roberto Leite<sup>3</sup>, Ernesto C. Pereira<sup>3</sup>, Elson Longo<sup>3</sup>, and Tatiana Martelli Mazzo<sup>2,\*</sup>

<sup>1</sup>Department of Chemistry, Universidade Estadual Paulista – Unesp, P.O. Box 473, Bauru, SP 17033-360, Brazil

<sup>2</sup>Institute of Marine Sciences, UNIFESP, Santos, SP 11070-102, Brazil

<sup>3</sup>LIEC – CDMF - Department of Chemistry, Universidade Federal de São Carlos, P.O. Box 676, São Carlos, SP 13565-905, Brazil

Received: 14 June 2019

Accepted: 15 October 2019

Published online:  
28 October 2019

© Springer Science+Business Media, LLC, part of Springer Nature 2019

## ABSTRACT

Because of the socio-environmental and economic impacts of the use of fossil fuels, the demand for the diversification of the energy matrix has increased. Energy devices utilizing renewable energy such as solar cells stand out as a possible solution to this problem. Therefore, in order to realize the practical applications of solar cells, it is imperative to develop novel structural materials and to optimize the properties of the existing ones. In this study, we prepared a photoelectrode using hematite-decorated zinc oxide particles (ZnO/Fe<sub>2</sub>O<sub>3</sub>). The field-emission scanning electron microscopy and Brunauer–Emmett–Teller results confirmed that Fe<sub>2</sub>O<sub>3</sub> coated the surface of the ZnO particles and improved their photoelectrochemical properties. The composite was found to be a promising photoelectrode for solar cells.

## Introduction

With the increasing concerns on environmental issues and the depletion of fossil fuels, the use of fossil fuel-based energy is being increasingly denigrated by modern society in order to adopt a sustainable lifestyle. The ease of dissemination of information due to globalization and the environmental awareness of people have made them

understand the negative impacts of these fuels. In this context, solar energy [1–3] is a promising alternative to fossil fuels because (1) it is environmentally friendly, (2) it is an abundant and unlimited source of energy, (3) different materials can be easily tailored to convert photons directly into electricity, and (4) it shows a wide range of applications [4, 5]. The use of solar energy has increased; however, its use still requires a high production cost because of the poor

Address correspondence to E-mail: tatimazzo@gmail.com

conversion efficiency of present day solar cells [6]. In order to overcome these limitations, various materials and methods have been developed to improve the production, efficiency, eco-friendliness, and cost-effectiveness of solar cells.

Zinc oxide (ZnO) is a promising material for solar cell applications. ZnO is a broadband semiconductor with a band gap of 3.3 eV at 300 K and a large exciton binding energy (60 meV) [7]. It crystallizes in the hexagonal wurtzite phase [8, 9]. Zn is abundantly available, and its oxide shows electronic mobility seven orders of magnitude higher than that of TiO<sub>2</sub> [10]. However, the power conversion efficiency of ZnO-based dye-sensitized solar cells (DSSCs) is lower than that of TiO<sub>2</sub>-based DSSCs because of the dissolution of ZnO and formation of dye-Zn<sup>2+</sup> aggregates in them and their lower injection efficiency [11].

On the other hand, hematite (Fe<sub>2</sub>O<sub>3</sub>) has been widely used as a photoanode material owing to its exceptional properties such as the band gap energy of 2.1 eV, highest theoretical efficiency (12.9%), good electrochemical stability, abundance, non-toxicity, and cost-effectiveness [11, 12]. However, it shows a short-excited state lifetime, small diffusion length, and low electrical conductivity [13, 14]. Doping with Ta [15], Ni [16], tC<sub>3</sub>N<sub>4</sub> [17], and Cr [18] is an efficient approach to improve the electrical conductivity of Fe<sub>2</sub>O<sub>3</sub> [18].

Dias et al. [19] evaluated the performance of hematite electrodes for photoelectrochemical water splitting. They adopted two strategies for the surface modification of hematite: (1) annealing at a high temperature (800 °C) and (2) coating with RuO<sub>2</sub> or IrO<sub>2</sub>/RuO<sub>2</sub>. The IrO<sub>2</sub>/RuO<sub>2</sub>-coated hematite photoanode exhibited the best performance with a photocurrent density of ca. 1.52 mA cm<sup>-2</sup> at 1.23 V<sub>RHE</sub>, which is 140% higher than that of pure hematite. It exhibited a photocurrent of 0.34 mA cm<sup>-2</sup> at 0.60 V<sub>RHE</sub>, which is the highest value ever reported. This photoelectrode showed a quite stable performance at 0.80 V<sub>RHE</sub> for over 72 h. It showed a water oxidation efficiency of more than 90% at potentials higher than 1.00 V<sub>RHE</sub> because of the rapid charge transfer and reduced electron–hole recombination at its surface.

Ikram et al. [20] investigated the photoelectrochemical performance of ZnO quantum dot (QD)-sensitized electrodeposited α-Fe<sub>2</sub>O<sub>3</sub> thin films prepared at various sensitization times. The ZnO QD sensitization increased the photocurrent of the Fe<sub>2</sub>O<sub>3</sub> thin films because of the efficient charge separation

caused by ZnO QDs and the catalytic behavior of ZnO.

Im et al. [21] used TiO<sub>2</sub>/Fe<sub>2</sub>O<sub>3</sub> as a photoelectrode material for DSSCs. The use of the TiO<sub>2</sub>/Fe<sub>2</sub>O<sub>3</sub> photoelectrodes improved the fill factor and efficiency of the DSSCs by more than 16% and 300%, respectively. This is because the conduction band of Fe<sub>2</sub>O<sub>3</sub> inhibited the trapping effect of the electrons in the conduction band of TiO<sub>2</sub>. This prevented the recombination of the electrons in the TiO<sub>2</sub> conduction band and the dye or electrolyte.

Considering all these aspects, in this study, we prepared hematite-decorated ZnO (ZnO/Fe<sub>2</sub>O<sub>3</sub>) particles and investigated their optical and electrochemical properties for a possible application as solar cell photoelectrodes.

## Methodology

### Synthesis of ZnO particles

The ZnO particles were prepared using a microwave-assisted hydrothermal method. Zinc nitrate (0.03 mol L<sup>-1</sup>) was dissolved in 50 mL of deionized water under constant stirring. To this solution, 50 mL of 2.0 mol L<sup>-1</sup> KOH was added, which resulted in the precipitation of particles. The resulting mixture was transferred to a Teflon reactor (reaction cup) with a volume of 110 mL. The reactor was then heated at 140 °C for 32 min in a modified microwave (MN-S46B) at a frequency and power of 2450 MHz and 1050 W, respectively. The microwave was controlled by a CNT400SUP v1.6 program. The product so obtained was washed with distilled water until a pH value of 7 was achieved. Finally, it was dried in an oven at 60 °C for 12 h.

### Synthesis of Fe<sub>2</sub>O<sub>3</sub> nanospheres

Iron oxide (Fe<sub>2</sub>O<sub>3</sub>) nanospheres with a uniform size and shape were synthesized via two steps: hydrothermal synthesis of the precursor and the subsequent calcination. Fe(NO<sub>3</sub>)<sub>3</sub>·9H<sub>2</sub>O (2.0 mmol), sodium citrate (4.0 mmol), and urea (5.0 mmol) were sequentially dissolved in 30 mL of deionized water under constant stirring. The clear yellow-green solution so obtained was placed in a reactor at 160 °C for 8 h. The solution was then cooled to room temperature. The brown precipitate so obtained was

washed with deionized water and isopropanol and was then dried in an oven at 60 °C for 4 h. The product was then heat-treated at 500 °C for 2 h to obtain a red powder [22].

### Preparation of ZnO and ZnO/Fe<sub>2</sub>O<sub>3</sub> photoelectrodes

The ZnO film was prepared by adding 0.20 g of ZnO to 1.0 mL of ethanol. This solution was sonicated for 30 min to obtain a ZnO dispersion. To this dispersion, 0.50 mL of deionized water was added and the resulting mixture was ultrasonicated for 30 min. Then, 80 μL of this mixture was dropped on a fluorine-doped oxide (FTO) substrate and was left at room temperature for 1 h for evaporating the solvent. The substrate was then calcined (to bind the film) at 400 °C for 1 h at the heating rate of 0.5 °C min<sup>-1</sup> to avoid the formation of cracks in the film [11]. The process of preparation of the ZnO/Fe<sub>2</sub>O<sub>3</sub> film was similar to that used for preparing the ZnO film. The only difference was that in the case of the ZnO/Fe<sub>2</sub>O<sub>3</sub> films, along with 0.20 g of ZnO, 20 μmol (1.57 wt %) of Fe<sub>2</sub>O<sub>3</sub> was also added to 1.0 mL of ethanol.

### Characterization

The properties of the samples (ZnO, Fe<sub>2</sub>O<sub>3</sub>, and ZnO/Fe<sub>2</sub>O<sub>3</sub>) were investigated by X-ray diffraction (XRD), field-emission scanning electron microscopy (FE-SEM), transmission electron microscopy (TEM), nitrogen adsorption–desorption isotherms, ultraviolet–visible (UV–Vis) absorption spectroscopy, photoluminescence (PL) spectroscopy, and photoelectrochemical measurements.

The XRD measurements were carried out using a D/Max-2500PC diffractometer (Rigaku) with Cu-K $\alpha$  radiation ( $\lambda = 1.5406 \text{ \AA}$ ). The XRD patterns were obtained over the  $2\theta$  range of 10°–110° at a scan rate of 0.02° min<sup>-1</sup>. The morphology of the samples was examined using FE-SEM (DSM 940/Zeiss). Transmission electron microscopy (TEM) images were taken using a FEI Tecnai F20 (Netherlands) microscope operating at 200 kV equipped with energy-dispersive X-ray spectrometer (EDS). The nitrogen adsorption–desorption isotherms of the samples were obtained at 77 K using a volumetric adsorption analyzer (TRISTAR II 3020/Micrometrics Instrument Corporation). Prior to their nitrogen adsorption–desorption isotherm measurements, the samples

were outgassed for 16 h at 573 K. The apparent surface area of the samples was measured using the Brunauer–Emmett–Teller (BET) equation [23, 24], while their pore size distribution was calculated using the Barrett–Joyner–Halenda (BJH) method with the adsorption branch [24]. The PL measurements of the samples were carried out in the UV–Vis region [25] using a 350-nm Kr laser (Coherent Innova). The output power was varied from 200 to 800 mW using suitable filters and prisms to remove the beam-loaded plasma. The width of the monochromator slot was 200 nm (Thermal Jarrell-Ash Monospec 27 model). The signal was detected using a R446 photomultiplier (Hamamatsu)-coupled SR-530 lock-in amplifier (SRS Products). All the measurements were carried out at room temperature. The UV–Vis absorption spectra of the samples were recorded in the total diffuse reflectance mode (Cary 5G, Varian). The photoelectrochemical measurements were carried out in a quartz glass cell with the three-electrode configuration. FTO/ZnO or FTO/ZnO/Fe<sub>2</sub>O<sub>3</sub> was used as the working electrode, the reference electrode was Ag/AgCl, and the counter electrode was Pt. The electrolytic solution consisted of acetonitrile (JT Baker), 10 mM of KI (Chemical Group), 1 mM of I<sub>2</sub> (Merck), and 0.1 M LiClO<sub>4</sub> (Merck). All the electrochemical tests were carried out on a potentiostat galvanostat (Autolab model 12/30302). The linear voltammetry curves of the samples were obtained over the potential range of 0.8–1.8 V at scan rate of 20 mV s<sup>-1</sup>. The tests were carried out in both the presence and absence of light (light/dark) using a solar simulator (Newport Sol3A Class AAA) with a 100-W xenon lamp. The stability of the samples (with respect to the current density) was evaluated by carrying out their chronoamperometry tests at a fixed potential of 1.2 V (optimized from linear voltammetry experiments) for 400 s.

### Results and discussion

The phases and crystallographic structures of all the samples were examined using XRD. Figure 1 shows the XRD patterns of pure ZnO, Fe<sub>2</sub>O<sub>3</sub>, and ZnO/Fe<sub>2</sub>O<sub>3</sub>.

The diffraction peaks of ZnO could be indexed to JCPDS 36-1451 [26, 27], indicating that it showed a hexagonal-type Wurtzite structure. In addition, the presence of well-defined and fine crystalline peaks

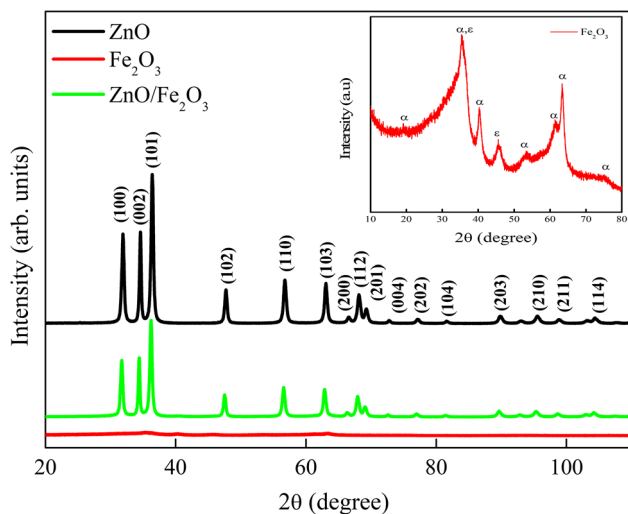


**Figure 1** XRD patterns of ZnO, Fe<sub>2</sub>O<sub>3</sub>, and ZnO/Fe<sub>2</sub>O<sub>3</sub>.

demonstrates the existence of a long-range structural order and non-existence of secondary phases. The Fe<sub>2</sub>O<sub>3</sub> samples (Fig. 1) showed peaks characteristic of nanostructured materials and a lower degree of crystallinity. However, their peaks could be indexed to  $\alpha$ -Fe<sub>2</sub>O<sub>3</sub> (ICSD #64599) and  $\epsilon$ -Fe<sub>2</sub>O<sub>3</sub> (ICSD #415250) [28, 29]. The ZnO/Fe<sub>2</sub>O<sub>3</sub> sample with fine and well-defined peaks showed a crystallographic profile similar to that of pure ZnO. The peaks corresponding to Fe<sub>2</sub>O<sub>3</sub> were absent in this case, suggesting that hematite was uniformly dispersed in the ZnO particles.

Thermogravimetric (TG) analysis was carried out to determine the decomposition temperatures of the samples and to examine their phase transformations. ATR-FTIR analysis was carried out to investigate the possible interaction between the ZnO particles and Fe<sub>2</sub>O<sub>3</sub> nanoparticles. Figure 2a, b shows the TG curves and ATR-FTIR spectra (over the 4000–480 cm<sup>-1</sup> range) of the ZnO, Fe<sub>2</sub>O<sub>3</sub>, and ZnO/Fe<sub>2</sub>O<sub>3</sub> samples, respectively.

The TG curve of pure ZnO showed (Fig. 2a) three weight-loss stages. The first weight loss at 50–200 °C was due to the desorption of water, low-molecular weight solvents/gases, and other degradation products. In the second stage, i.e., at 200–500 °C, the weight loss was caused by the decomposition of the species adsorbed on the oxide surface. The third weight-loss stage initiated at 513 °C and can be attributed to the decomposition of hydrocarbonate products. The TG curve of Fe<sub>2</sub>O<sub>3</sub> (Fig. 2a) also showed three weight-loss stages. The first stage was

observed at 25–150 °C and can be attributed to the dehydration of the sample. The weight loss at 150–300 °C (second stage) corresponds to the degradation of residual nitrate. In the last stage, gradual weight loss was observed at temperatures above 300 °C, indicating the transformation of the unwanted phases. This indicates that the calcination temperature of 500 °C was not sufficient to obtain pure Fe<sub>2</sub>O<sub>3</sub> particles. This result is in agreement with the XRD analysis (Fig. 1), which shows that the alpha ( $\alpha$ ) and epsilon ( $\epsilon$ ) phases of Fe<sub>2</sub>O<sub>3</sub> are present. The ZnO/Fe<sub>2</sub>O<sub>3</sub> sample (Fig. 2a) showed the same weight-loss profile as that of pure ZnO. However, the weight loss in each stage was higher (by 0.5, 0.4, and 0.6% in the first, second, and third stages, respectively) in the case of the ZnO/Fe<sub>2</sub>O<sub>3</sub> sample. This indicates that the addition of Fe<sub>2</sub>O<sub>3</sub> slightly increased the degradation temperature of the ZnO particles.

The ATR-FTIR spectrum of the ZnO particles (Fig. 2b) showed bands at 480–590 cm<sup>-1</sup> corresponding to the stretching vibration of ZnO. The ATR-FTIR spectrum of the Fe<sub>2</sub>O<sub>3</sub> particles (Fig. 2b) showed a broad band at 3362 cm<sup>-1</sup> corresponding to the water molecules coordinated in the lattice in the form of hydroxide (OH stretching). The bands at 1618 and 1400 cm<sup>-1</sup> can be assigned to the bending vibration of the OH group and the in-plane OH bending, respectively. The band at 900 cm<sup>-1</sup> can be attributed to the oxide phases (FeO or FeO<sub>2</sub> among others). It is well known that iron exists in more than one oxidation states. Hence, until the formation of the Fe<sub>2</sub>O<sub>3</sub> product, it existed in various oxide phases [30]. The ATR-FTIR results were consistent with XRD and TG analysis results, indicating that the calcination temperature was not sufficient to obtain a pure Fe<sub>2</sub>O<sub>3</sub> sample. The band at 545 cm<sup>-1</sup> corresponds to the Fe–O stretching vibration mode of Fe<sub>2</sub>O<sub>3</sub> [31, 32]. Like Fe<sub>2</sub>O<sub>3</sub>, the ZnO/Fe<sub>2</sub>O<sub>3</sub> sample showed a band at 900 cm<sup>-1</sup> but with lower intensity, indicating the presence of some iron oxide phases in it. The increase in the intensity of the bands at 480–590 cm<sup>-1</sup> corresponds to the increase in the metal oxide content.

Figure 2c shows the Raman spectra of ZnO, Fe<sub>2</sub>O<sub>3</sub> and ZnO/Fe<sub>2</sub>O<sub>3</sub>. The Raman spectrum of ZnO showed optical phonons at the  $\Gamma$  point of the Brillouin zone corresponding to the irreducible relation:  $\Gamma_{\text{opt}} = A_1 + E_1 + 2E_2 + 2B_1$ . The  $A_1$  and  $E_1$  modes split into transverse (TO) and longitudinal optical (LO) phonons, while the  $E_2$  modes were non-polar.  $A_1$  and  $E_1$  modes are Raman and infrared active,



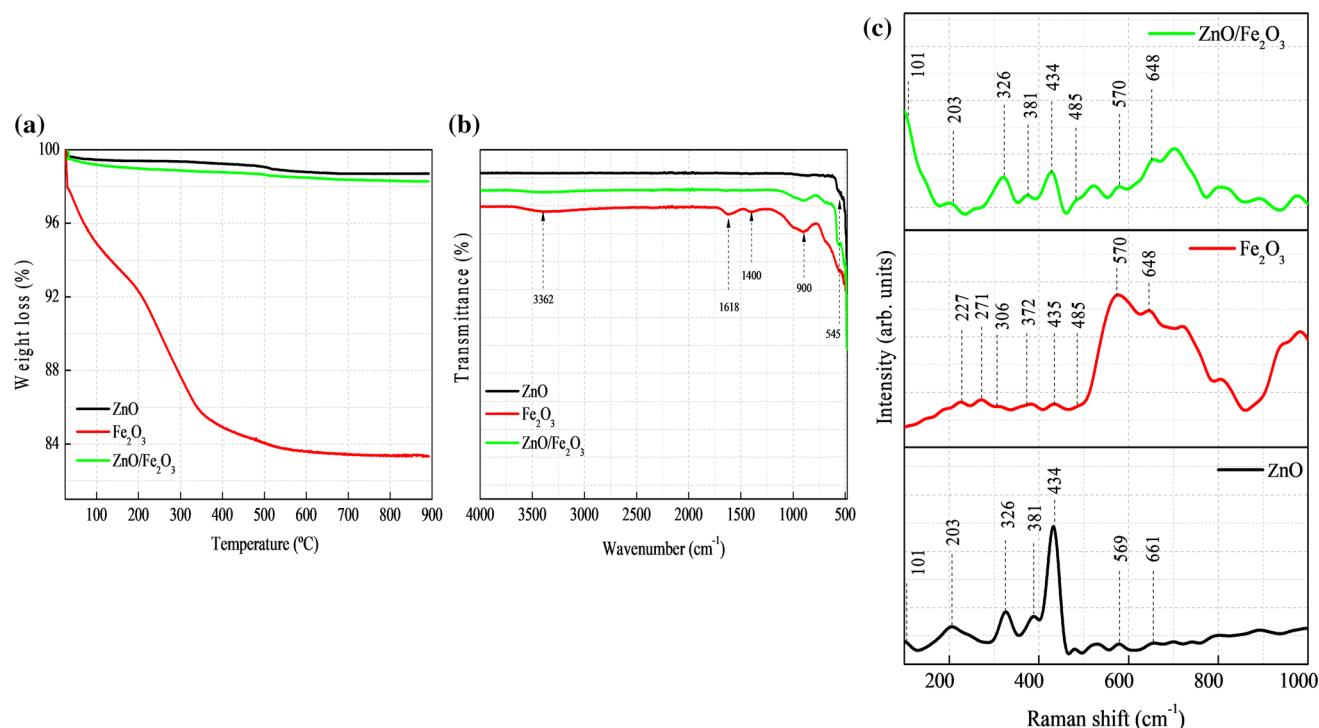


**Figure 2** TG analysis (a), ATR-FTIR spectra (b), and Raman spectra (c) of ZnO, Fe<sub>2</sub>O<sub>3</sub>, and ZnO/Fe<sub>2</sub>O<sub>3</sub>.

while E<sub>2</sub> modes are only Raman active. B<sub>1</sub> modes are Raman and infrared inactive [33]. The allowed backscattering geometry modes appeared in the E<sub>2</sub> (low and high) mode at 101 and 434 cm<sup>-1</sup>, indicating the excellent quality of the crystal [34, 35]. The peak at 381 cm<sup>-1</sup> corresponds to the A<sub>1</sub> (TO) mode, while those at 203 and 326 cm<sup>-1</sup> can be assigned to the acoustic phonon and optical phonon overtones with the A<sub>1</sub> symmetry, respectively [36]. The Raman mode at 569 cm<sup>-1</sup> corresponds to the E<sub>1</sub> (LO) mode of ZnO [33]. The peak at 661 cm<sup>-1</sup> corresponds to the additional vibrational modes associated with defects [37]. Figure 2c (red line) shows the Raman spectrum of Fe<sub>2</sub>O<sub>3</sub>. The spectrum showed seven phonon modes predicted by the group theory and Raman-inactive and IR-active E<sub>u</sub> (LO) modes [38]. The Raman modes at 227, 271, 306, 372, 435, 485, 570, and 648 cm<sup>-1</sup> correspond to A<sub>1g</sub>, E<sub>g</sub>, E<sub>g</sub>, E<sub>g</sub>, E<sub>g</sub>, A<sub>1g</sub>, E<sub>g</sub>, and E<sub>u</sub> respectively. The ZnO particles decorated with the Fe<sub>2</sub>O<sub>3</sub> particles showed Raman modes at 101, 203, 326, 381, and 434 cm<sup>-1</sup> corresponding to the lattice vibrations of the ZnO structure. These particles also showed Raman modes at 485, 570, and 648 cm<sup>-1</sup> corresponding to the lattice vibrations of the Fe<sub>2</sub>O<sub>3</sub> nanostructure. This confirms that the ZnO particles were successfully decorated with the Fe<sub>2</sub>O<sub>3</sub> particles.

Figure 3 (I) shows the FE-SEM images, and Fig. 3 (II) displays the histograms of particles size of all the samples.

Figure 3 (I) a, b shows the FE-SEM images of the FTO substrate. From the images, it can be observed that the FTO substrate consisted of uniformly arranged nanoparticles with a diameter of 50–300 nm. These particles rendered the substrate surface rough. This is consistent with the results reported previously [39]. Figure 3 (I) c–e shows the FE-SEM images of the pure ZnO particles deposited on the FTO substrate. It can be observed that these particles showed a flower-type structure and consisted of “micro-petals.” These flowers had a diameter of 447–3561 nm. These particles were porous and showed a large surface area because of the presence of their petal-like shape. Figure 3 (I) f, g shows the FE-SEM images of the Fe<sub>2</sub>O<sub>3</sub> nanoparticles. These nanoparticles were spherical and resembled monodisperse spheres [40]. Figure 3 (I) h–j shows the FE-SEM images of the ZnO/Fe<sub>2</sub>O<sub>3</sub> composite. From these images, it can be observed that the Fe<sub>2</sub>O<sub>3</sub> nanospheres were successfully incorporated into the flower structure of ZnO (Fig. 3 (I) e, j) because of its large size and porosity and the large surface area of its micro-petals. This

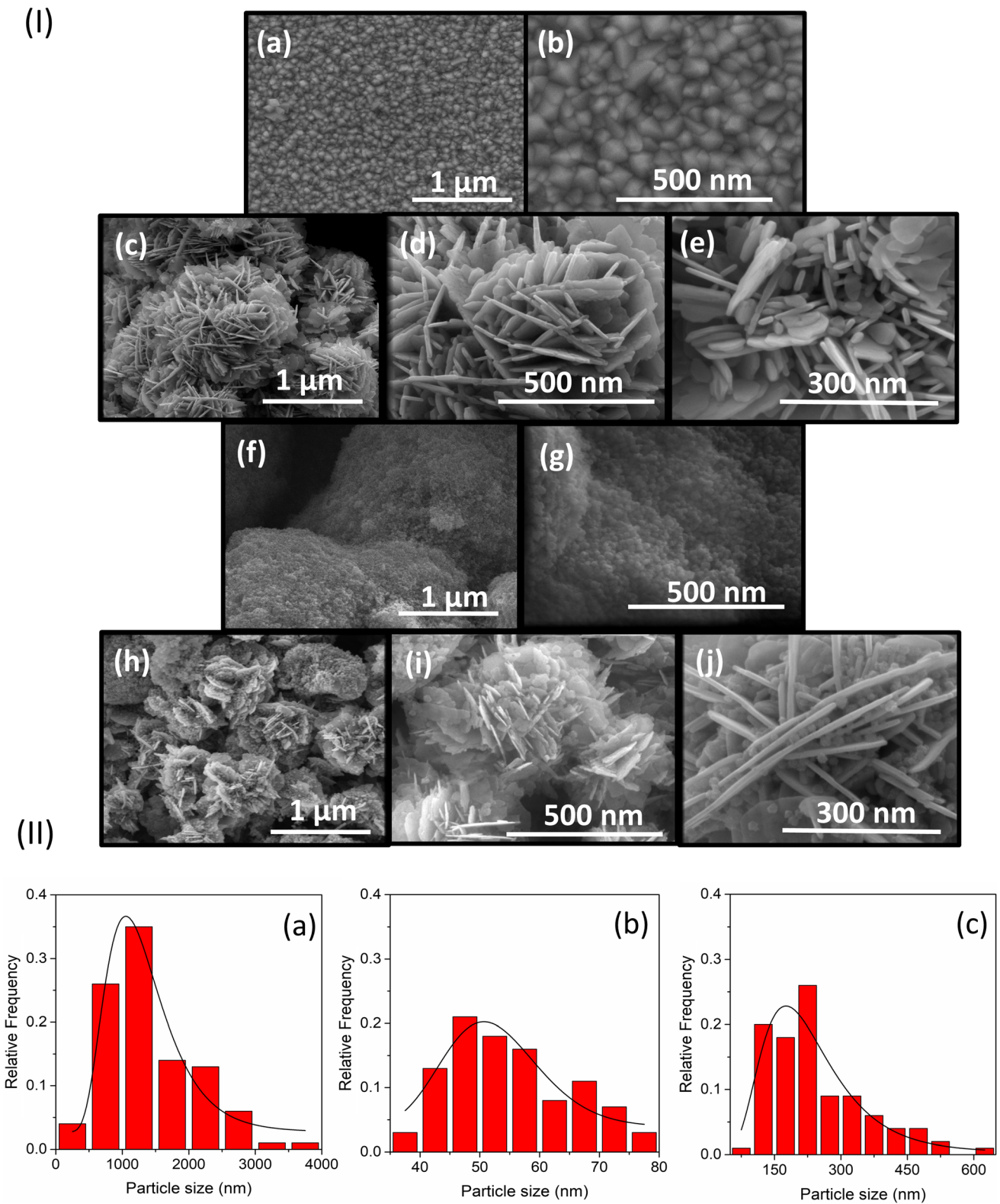


**Figure 3** FE-SEM images of FTO (I) a–b, ZnO (I) c–e, Fe<sub>2</sub>O<sub>3</sub> f–g, and ZnO/Fe<sub>2</sub>O<sub>3</sub> (I) h–j, and particle sizes of ZnO (II) a, Fe<sub>2</sub>O<sub>3</sub> (II) b, and ZnO/Fe<sub>2</sub>O<sub>3</sub> (II) c.

resulted in the sensitization of ZnO by Fe<sub>2</sub>O<sub>3</sub>. Hence, it can be stated that hematite played the role of a dye.

From the FE-SEM images, it can be observed that pure ZnO and ZnO/Fe<sub>2</sub>O<sub>3</sub> showed the same microflower-like morphology. However, the addition of Fe<sub>2</sub>O<sub>3</sub> resulted in the coalescence of the nanostructure. This can be attributed to the decrease in the mean size of the ZnO micro-petals with the addition of hematite. Figure 3 (II) a–c shows the relative frequency versus particle size histograms of the samples. It can be observed that the addition of the Fe<sub>2</sub>O<sub>3</sub> nanoparticles reduced the size of the ZnO micro-petals by approximately 5.8 times.

Figure 4 shows the TEM images and chemical composition of ZnO, Fe<sub>2</sub>O<sub>3</sub> and ZnO/Fe<sub>2</sub>O<sub>3</sub> samples.

The morphology of ZnO, Fe<sub>2</sub>O<sub>3</sub>, and the composite sample was investigated by TEM, as shown in Fig. 4 a–c, respectively. A close observation of ZnO/Fe<sub>2</sub>O<sub>3</sub> sample (Fig. 4c) shows that indeed the ZnO particles were decorated by Fe<sub>2</sub>O<sub>3</sub> nanoparticles. The elemental microanalysis results performed by EDS for all samples (Fig. 4) proved the chemical composition of ZnO, Fe<sub>2</sub>O<sub>3</sub> and ZnO/Fe<sub>2</sub>O<sub>3</sub> materials. The presence of Ni observed in the pure ZnO sample is relative to the TEM grid.

Figure 5 displays the high-resolution TEM (HRTEM) image and selective area electron diffraction (SAED) pattern of ZnO and ZnO/Fe<sub>2</sub>O<sub>3</sub> samples.

Figure 5a shows the HRTEM image with an overview of ZnO petals and in the delimited region a SAED image of pure ZnO was obtained. These results reveal the polycrystalline wurtzite ZnO structure. The indexed planes showed that the symmetry was ZnO phase with space group P63mc. The SAED image of the ZnO/Fe<sub>2</sub>O<sub>3</sub> sample (Fig. 5b) indicated that the ZnO particles decorated have the same planes and phase symmetry as the pure ZnO. The Fe<sub>2</sub>O<sub>3</sub> particles were polycrystalline, and the SAED images also showed α-Fe<sub>2</sub>O<sub>3</sub> and ε-Fe<sub>2</sub>O<sub>3</sub> phases with space group R-3c and Pna-21, respectively. This is in accordance with XRD, TG and FTIR analyzes. The results obtained from the HRTEM images confirmed that the ZnO particles were successfully decorated by the Fe<sub>2</sub>O<sub>3</sub> nanoparticles. The SAED images indicated the formation of heterojunction between ZnO and Fe<sub>2</sub>O<sub>3</sub>, since the symmetry of the crystallographic phases was maintained.

The specific surface areas and pore volumes of ZnO and ZnO/Fe<sub>2</sub>O<sub>3</sub> were determined by obtaining their nitrogen adsorption–desorption isotherms at 77 K (Table 1).

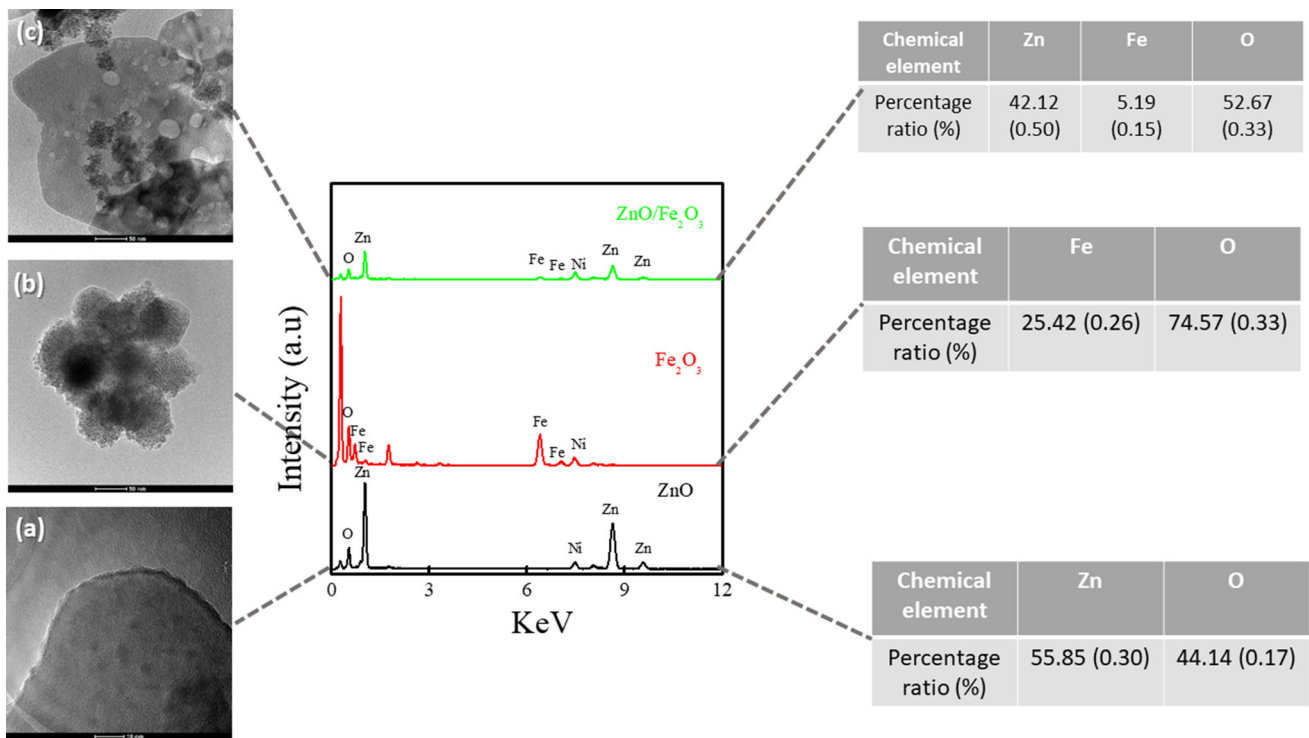


**Figure 4** TEM images and chemical composition of ZnO (a), Fe<sub>2</sub>O<sub>3</sub> (b), and ZnO/Fe<sub>2</sub>O<sub>3</sub> (c).



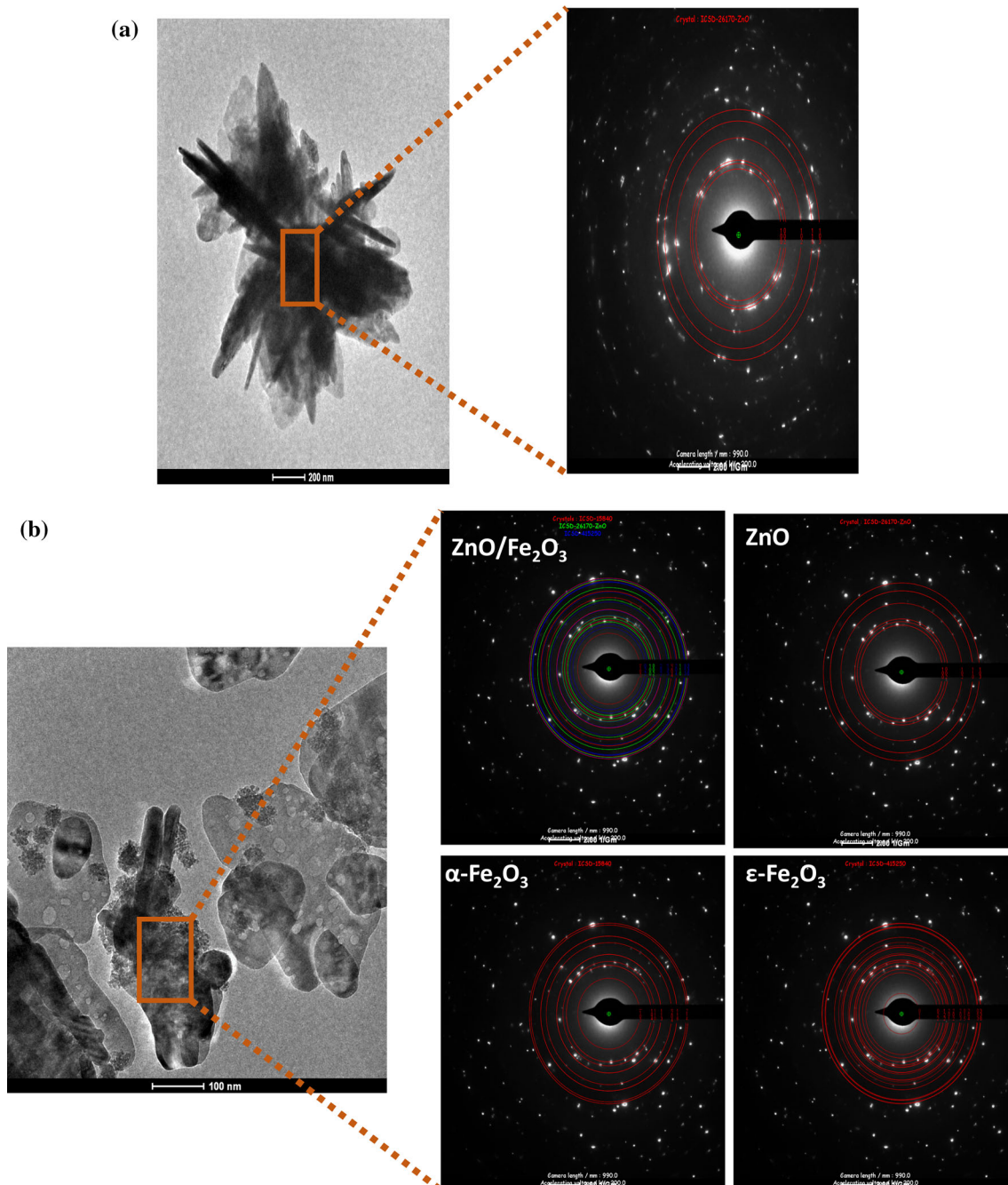


**Figure 5** High-resolution TEM (HRTEM) image and selective area electron diffraction (SAED) pattern of ZnO (a) and ZnO/Fe<sub>2</sub>O<sub>3</sub> (b) samples.

**Table 1** Surface areas and pore sizes of ZnO and ZnO/Fe<sub>2</sub>O<sub>3</sub>

Sample	BET surface area (m <sup>2</sup> g <sup>-1</sup> )	Pore volume (cm <sup>3</sup> g <sup>-1</sup> )
ZnO	13.0	0.06
ZnO/Fe <sub>2</sub> O <sub>3</sub>	32.5	0.12



The surface area of the ZnO particles increased significantly with the addition of Fe<sub>2</sub>O<sub>3</sub>. The addition of Fe<sub>2</sub>O<sub>3</sub> increased the pore volume of the ZnO particles by two times. This explains the increase in their surface area. Thus, because of their small pores (micro and meso) the hematite-decorated ZnO particles showed a large surface area and hence a large exposed active region for electrochemical reactions. This indicates that a large amount of Fe<sub>2</sub>O<sub>3</sub> was loaded on the ZnO particles.

The band gap energy of the samples and the possible mechanism to the improvement of the photoelectrochemical property of ZnO/Fe<sub>2</sub>O<sub>3</sub> are shown in Fig. 6.

UV–Vis spectroscopic measurements were carried out to investigate the effect of the addition of the

Fe<sub>2</sub>O<sub>3</sub> particles on the optical properties of pure ZnO. The band gap energies ( $E_g$ , eV) of the samples were calculated from their UV–Vis data using the Kubelka and Munk method [41] as follows:

$$\alpha hv = A(hv - E_g)^n \tag{1}$$

where  $\alpha$  is the linear absorption coefficient of the material,  $h\nu$  is the incident photon energy,  $A$  is a proportionality constant related to the material,  $E_g$  is the band gap energy of the semiconductor, and  $n$  is a constant depending on the type of electronic transitions ( $n = 1/2$  for a direct allowed transition;  $n = 2$  for an indirect allowed transition).

ZnO is an  $n$ -type direct band gap semiconductor with  $n = 1/2$  [42]. The direct band gap energies of the

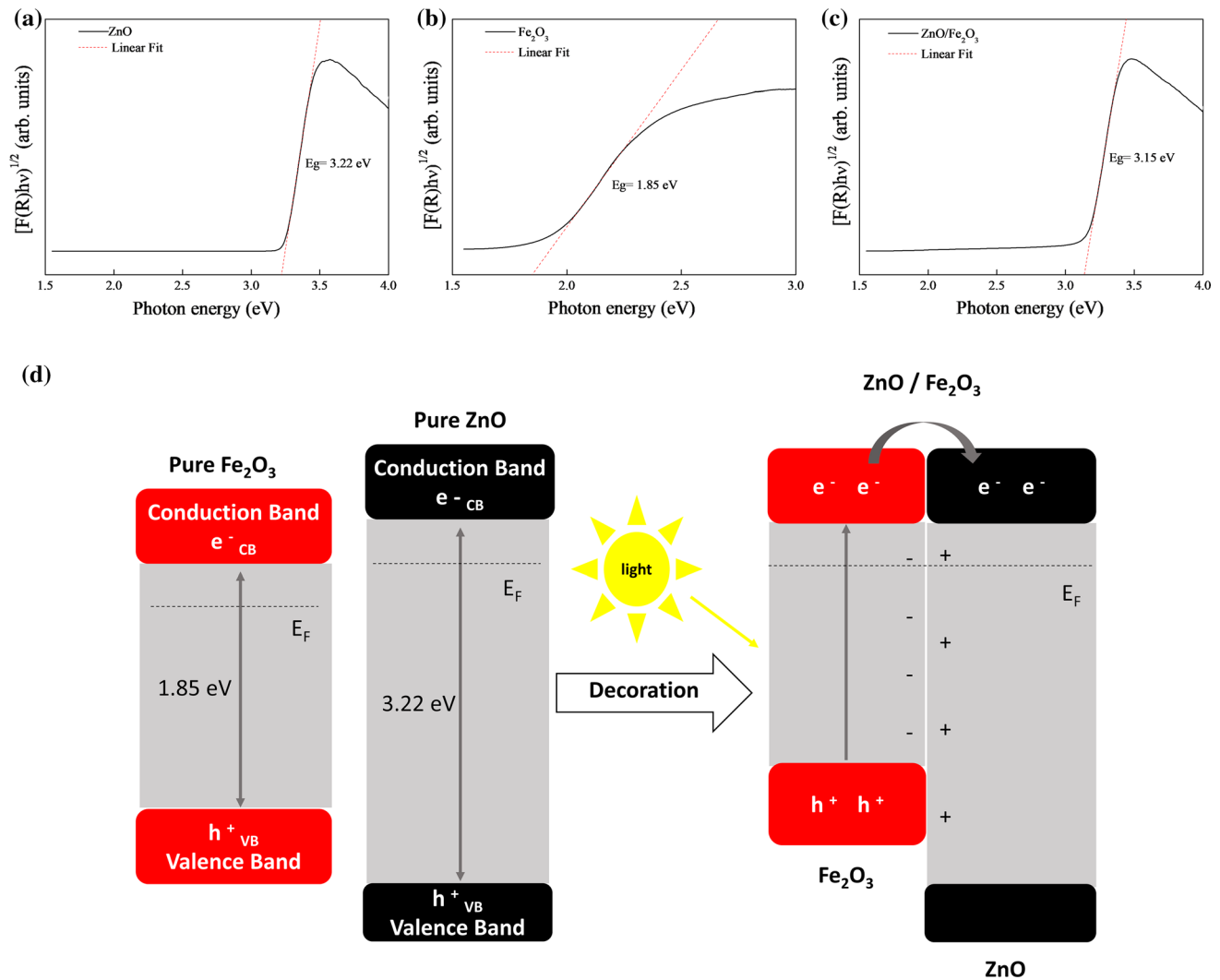


**Figure 6** Band gap energy of ZnO (a), Fe<sub>2</sub>O<sub>3</sub> (b), and ZnO/Fe<sub>2</sub>O<sub>3</sub> (c) and possible mechanism to the improvement of the photoelectrochemical property of ZnO/Fe<sub>2</sub>O<sub>3</sub> (d).

samples are shown in Fig. 6. The band gap values of ZnO, Fe<sub>2</sub>O<sub>3</sub>, and ZnO/Fe<sub>2</sub>O<sub>3</sub> were 3.22, 1.85, and 3.15 eV, respectively. ZnO and ZnO/Fe<sub>2</sub>O<sub>3</sub> showed similar  $E_g$  values. This is consistent with the XRD results.

Figure 6d presents the possible mechanism for the improving in the photoelectrochemical property presented by the ZnO/Fe<sub>2</sub>O<sub>3</sub> sample. ZnO has a band gap of 3.22 eV, which makes it active only when exposed to UV light [43]. On the other hand, Fe<sub>2</sub>O<sub>3</sub> has a 1.85 eV band gap, having a good visible light response [44]. When ZnO is decorated with Fe<sub>2</sub>O<sub>3</sub>, this mixture can become active for visible light and improve separation of the photoinduced charge carriers. This improvement can be attributed to the formation of an *n-n* semiconductor heterojunction between ZnO and Fe<sub>2</sub>O<sub>3</sub> [45]. After the heterojunction formation, electrons ( $e^-$ ) can migrate from the Fermi level ( $E_F$ ) of ZnO to Fe<sub>2</sub>O<sub>3</sub> until their  $E_F$  are equal. This process leads to the generation of positive charge in the junction area of ZnO and negative charges over Fe<sub>2</sub>O<sub>3</sub>. When the ZnO/Fe<sub>2</sub>O<sub>3</sub> sample is exposed to visible light, the photogenerated electrons ( $e^-$ ) in the Fe<sub>2</sub>O<sub>3</sub> conduction band (CB) can migrate to ZnO and the holes ( $h^+$ ) remain in the Fe<sub>2</sub>O<sub>3</sub> valence band (VB), resulting in the separation of the charge carriers. Therefore, the improvement in the photoelectrochemical performance of ZnO/Fe<sub>2</sub>O<sub>3</sub> sample can be attributed to the formation of *n-n* heterojunction and the separation of charge carriers.

Figure 7 shows the PL spectra of ZnO, Fe<sub>2</sub>O<sub>3</sub>, and ZnO/Fe<sub>2</sub>O<sub>3</sub> at room temperature.

From Fig. 7a, it can be observed that the PL spectrum of pure ZnO consists mainly of two bands of emissions. The broad peak in the visible blue region (3.0–3.5 eV) can be attributed to the intrinsic defects such as zinc vacancies ( $V_{Zn}$ ), interstitial zinc ( $Zn_i$ ), singly negatively charged Zn vacancies ( $V_{Zn}^-$ ), and oxygen vacancies ( $V_O$ ) [46–49]. The second emission band of ZnO has maximum intensity of PL at 620 nm (2.0 eV). This value was consistent with those reported previously [50]. However, the emission in the blue region was suppressed after the ZnO particles decoration by Fe<sub>2</sub>O<sub>3</sub>, suggesting a decrease in the concentrations of the point defects mentioned above. The intensity of PL band also decreases when the ZnO particles were decorated with Fe<sub>2</sub>O<sub>3</sub> and the PL emission in the visible spectrum displayed a maximum intensity at 663 nm (1.87 eV). This behavior indicates a reduction of the density of intrinsic

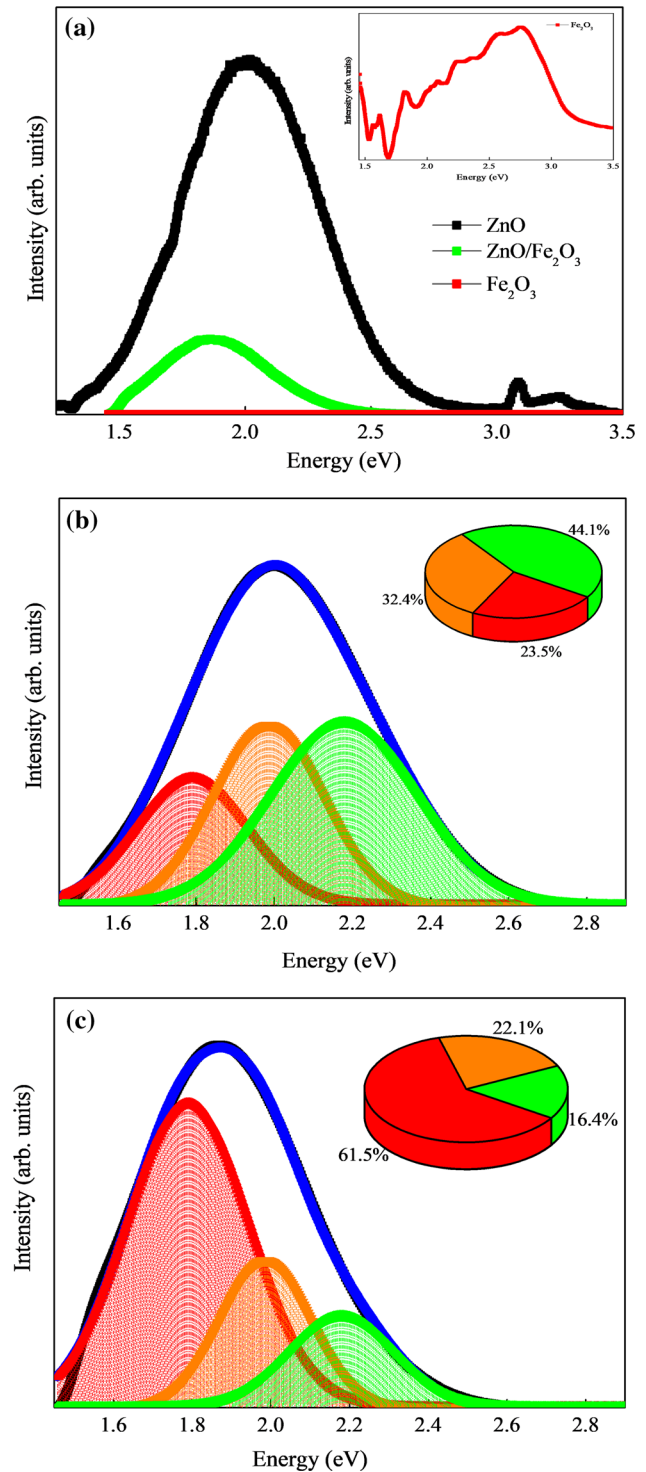


**Figure 7** PL curve and deconvolution of the three PL peaks of ZnO (b) and ZnO/Fe<sub>2</sub>O<sub>3</sub> (c).

defects in ZnO with Fe<sub>2</sub>O<sub>3</sub> addition. However, it can evidence the band gap reduction by the formation of (Fe<sub>Zn</sub>-V<sub>Zn</sub>) complexes where the energy levels are localized near the valence band [51]. This reduction

in band gap was observed (Fig. 6), thus indicating the formation of  $(\text{Fe}_{\text{Zn}}-\text{V}_{\text{Zn}})$  complexes. However, the  $\text{Fe}_2\text{O}_3$  sample did not show significant emission over the energy range used in this study. Figure 7b, c shows the deconvolution of the three peaks of the pure ZnO and ZnO/ $\text{Fe}_2\text{O}_3$  samples. The PL spectrum of pure ZnO showed three emission peaks at 2.0 (orange), 1.80 (red), and 2.18 eV (green) (Fig. 7b). The PL deconvolution results showed that the emission of the pure ZnO sample was the highest in the green region (44.1%). This can be attributed to the recombination of the isolated electrons in the ionized oxygen vacancies ( $\text{V}_{\text{O}}$ ) with photogenerated holes [52]. Figure 7c shows the PL spectrum of ZnO/ $\text{Fe}_2\text{O}_3$ . The spectrum consisted of three components located at the same energy values as those of pure ZnO. The deconvolution results showed a shift in the maximum emission for the red region (61.5%). This is because the addition of  $\text{Fe}_2\text{O}_3$  reduced the concentration of shallow defects in ZnO, thus giving rise to deep defects. This is because the calcination time of 2 h was not enough for the formation of pure and organized hematite crystals, as revealed by the XRD, FTIR, TG and TEM results. Materials with low degrees of structural organization exhibit a large number of structural distortions and/or defects (vacancies). Moreover, the luminescence of a material is caused by the recombination of the electrons in the “holes” of the valence band generated by their excitation toward the conduction band. Therefore, the presence of these defects facilitates the accommodation of electrons in different energy states, thus altering the photoluminescent behavior of the material, which in many cases increases its luminescent emission capacity [53].

Figure 8 shows the linear voltammetry results of the pure ZnO and ZnO/ $\text{Fe}_2\text{O}_3$  films.

Figure 8 shows that the current density of the samples started increasing at the potential of 1.0 V. The ZnO/ $\text{Fe}_2\text{O}_3$  sample showed the highest current density of  $0.77 \text{ mA cm}^{-2}$  at 1.2 V in the presence of light. Under the dark condition, pure ZnO showed a current density of  $0.16 \text{ mA cm}^{-2}$ , which is higher than that obtained in the presence of light. This indicates that its stability decreased upon excitation by photons. Hence, it can be stated that the addition of  $\text{Fe}_2\text{O}_3$  increased the current density of the pure ZnO film under both the light and dark conditions to approximately  $0.61 \text{ mA cm}^{-2}$ , which is considered to be desirable for solar cell applications. The difference

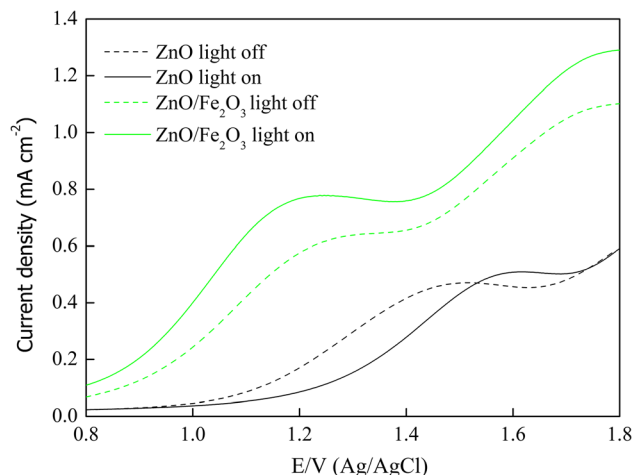


**Figure 8** J–V characteristics of the ZnO and ZnO/ $\text{Fe}_2\text{O}_3$  samples recorded in acetonitrile with 10 mM LiI, 1 mM  $\text{I}_2$ , and 0.1 M  $\text{LiClO}_4$  in the dark (dashed lines) and under light (solid lines).

in the current density values of pure ZnO obtained in this study and the ZnO photoelectrodes reported previously was found to be  $0.005\text{--}0.007 \text{ mA cm}^{-2}$  [10] or  $0.12\text{--}0.23 \text{ mA cm}^{-2}$  [50]. This indicates that the current density value obtained in this study was consistent with those reported previously. The results demonstrated the advantages of the addition of  $\text{Fe}_2\text{O}_3$  to ZnO for photoelectrochemical applications.

The photoresponse properties of the FTO/ZnO/ $\text{Fe}_2\text{O}_3$  electrodes were investigated at 1.2 V versus Ag/AgCl for a duration of 0–400 s (Fig. 9).

From Fig. 9, it can be observed that the two electrodes showed an atypical spike in their

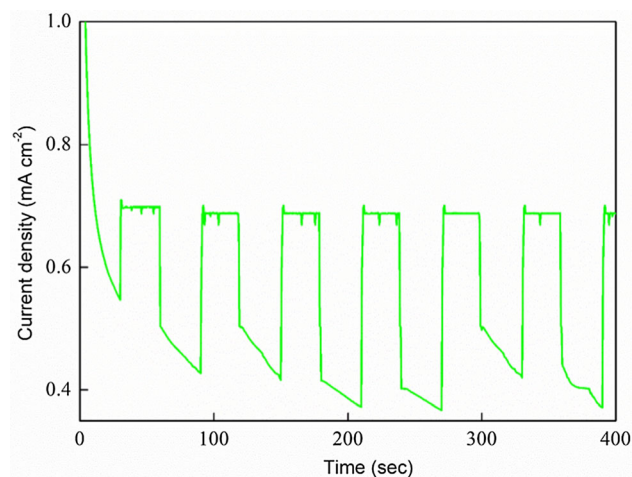
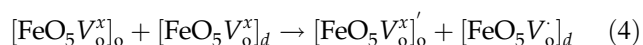
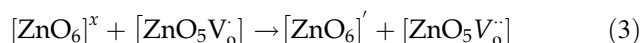
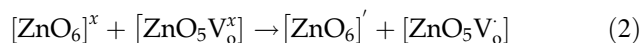


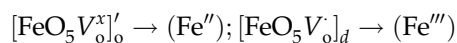
**Figure 9** Photoactivation current measured at the applied potential of 1.2 V versus Ag/AgCl for ZnO/ $\text{Fe}_2\text{O}_3$  under Xe light illumination in acetonitrile with 10 mM LiI, 1 mM  $\text{I}_2$ , and 0.1 M  $\text{LiClO}_4$ .

photoresponse owing to the transient effect of power excitation. The photocurrent then quickly returned to a steady state. This can be attributed to the fast recombination on the surface of the photoelectrodes because of their limited hole–electron pair lifetimes and poor minority carriers [52]. The FTO/ZnO/Fe<sub>2</sub>O<sub>3</sub> electrode showed a current density of 0.70 mA cm<sup>-2</sup> when exposed to light. This current density was about 1.75 times higher than that obtained under the dark condition.

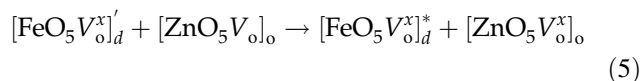
We believe that the main reason for this enhanced photoresponse was the coupling between the states in the complex clusters of [FeO<sub>5</sub>]<sub>o</sub><sup>x</sup>/[FeO<sub>5</sub>]<sub>d</sub><sup>x</sup> and the defects of [ZnO<sub>6</sub>]<sup>x</sup>/[ZnO<sub>5</sub>V<sub>o</sub>]<sup>x</sup>. ZnO couples with the complex clusters of tin oxide as follows:



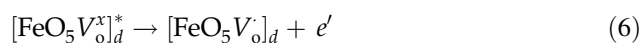
where



Complex clusters excitation:



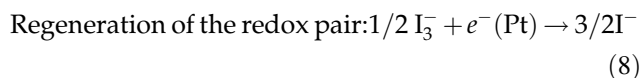
Injection of electrons:



Thus, the reduction of iodide ions (I<sup>-</sup>), which are present in the liquid electrolyte along with triiodide ions (I<sub>3</sub><sup>-</sup>), is carried out in order to regenerate the oxidized cluster (FeO<sub>5</sub>).



The photogenerated electrons are then transported through the external circuit, where they perform work and reach the counter electrode to reduce the triiodide ions (I<sub>3</sub><sup>-</sup>) to I<sup>-</sup> (Eq. 8):



## Conclusion

The results of the physicochemical and photoelectrochemical examinations obtained by us in this study showed that ZnO/Fe<sub>2</sub>O<sub>3</sub> composites are promising candidates for solar cell photoelectrodes applications owing to their high current density and stability (as compared to pure ZnO). The Fe<sub>2</sub>O<sub>3</sub> nanoparticles, which were used for decorating the ZnO film, played the role of a coloring material because of their interaction with the ZnO particles. The current values of the electrodes prepared in this study were higher than those reported previously (fully assembled and decorated). Moreover, the microwave-assisted method used in this study to prepare the ZnO/Fe<sub>2</sub>O<sub>3</sub> composite reduced the production cost since it did not require sophisticated equipment and high energy. The method also reduced the processing time and did not produce any by-product and hence is a promising approach for the preparation of such composites.

## Acknowledgements

This study was financed in part by the São Paulo Research Foundation - FAPESP (2013/07296-2), Coordenação de Aperfeiçoamento de Pessoal de Nível Superior - Brasil (CAPES) - Finance Code 001 and Conselho Nacional de Desenvolvimento Científico e Tecnológico (CNPq).

## References

- [1] Dresselhaus MS, Thomas IL (2001) Alternative energy technologies. *Nature* 414:332–337
- [2] Pearce JM (2002) Photovoltaics—a path to sustainable futures. *Futures* 34:663–674
- [3] Modi A, Bühler F, Andreasen JG, Haglind F (2017) A review of solar energy based heat and power generation systems. *Renew Sustain Energy Rev* 67:1047–1064
- [4] Mekhilef S, Saidur R, Safari A (2011) A review on solar energy use in industries. *Renew Sustain Energy Rev* 5:1777–1790
- [5] Lof GOG (1960) Profits in Solar Energy. *Solar. Energy* 4:9–15
- [6] Koroneos C, Spachos T, Moussiopoulos N (2003) Exergy analysis of renewable energy sources. *Renew Energy* 28:295–310



- [7] Janotti A, Van de Walle CG (2009) Fundamentals of zinc oxide as a semiconductor. *Rep Prog Phys* 72:126501
- [8] Marimuthu T, Anandhan N, Thangamuthu R, Surya S (2017) Facile growth of ZnO nanowire arrays and nanoneedle arrays with flower structure on ZnO–TiO<sub>2</sub> seed layer for DSSC applications. *J Alloys Comp* 693:011–1019
- [9] Klingshirn CF (2007) ZnO: material, physics and applications. *Chem Phys Chem* 8:782–803
- [10] Chava RK, Kang M (2017) Improving the photovoltaic conversion efficiency of ZnO based dye sensitized solar cells by indium doping. *J Alloys Comp* 692:67–76
- [11] Çakar S, Özacar M (2016) Fe-tannic acid complex dye as photo sensitizer for different morphological ZnO based DSSCs. *Spectrochim A* 163:79–88
- [12] Shinde PS, Geun HO, Won JL (2012) Facile growth of hierarchical hematite ( $\alpha$ -Fe<sub>2</sub>O<sub>3</sub>) nanopetals on FTO by pulse reverse electrodeposition for photoelectrochemical water splitting. *Mater Chem* 22:0469–10471
- [13] Sivula K, Zboril R, Formal FL, Robert R, Weidenkaff A, Tucek J, Frydrych J, Gratzel M (2010) Photoelectrochemical water splitting with mesoporous hematite prepared by a solution-based colloidal approach. *J Am Chem Soc* 132:7436–7444
- [14] Wang G, Ling Y, Damon A, Kyle ENG, Kimberly H, Clemens H, Zhang JZ, Li Y (2011) Facile synthesis of highly photoactive  $\alpha$ -Fe<sub>2</sub>O<sub>3</sub>-based films for water oxidation. *Nano Lett* 11:2119–2125
- [15] Huicheng L, Dongfang N, Deying L, Wenjiao H, Xinsheng Z (2017) Understanding the enhanced photoelectrochemical activity of Ta doped hematite. *J Mol Struct* 1139:104–110
- [16] Phuan YW, Ibrahim E, Chong MN, Zhua T, Lee BK, Ocon JD, Chan ES (2017) In situ Ni-doping during cathodic electrodeposition of hematite for excellent photoelectrochemical performance of nanostructured nickel oxide-hematite p-n junction photoanode. *Appl Surf Sci* 392:144–152
- [17] Arora P, Singh AP, Mehta BR, Basu S, Vacuum (2017) Metal doped tubular carbon nitride (tC3N4) based hematite photoanode for enhanced photoelectrochemical performance. *Vacuum* 146:570–577
- [18] Linsen L, Yanghai Y, Fei M, Yizheng T, Robert JH, Song J (2012) Facile solution synthesis of  $\alpha$ -FeF<sub>3</sub>·3H<sub>2</sub>O nanowires and their conversion to  $\alpha$ -Fe<sub>2</sub>O<sub>3</sub> nanowires for photoelectrochemical application. *Nano Lett* 12:724–731
- [19] Dias P, Andrade L, Mendes A (2017) Hematite-based photoelectrode for solar water splitting with very high photovoltage. *Nano Energy* 38:218–231
- [20] Ikram A, Sahai A, Rai S, Dass S, Shrivastav R, Satsangi VR (2015) Enhanced photoelectrochemical conversion performance of ZnO quantum dots sensitized  $\alpha$ -Fe<sub>2</sub>O<sub>3</sub> thin films. *J Hydrog Energy* 40:5583–5592
- [21] Ji SI, Sung KL, Young-Seak L (2011) Cocktail effect of Fe<sub>2</sub>O<sub>3</sub> and TiO<sub>2</sub> semiconductors for a high performance dye-sensitized solar cell. *Appl Surf Sci* 257:2164–2169
- [22] Gou X, Wang G, Park J, Liu H, Yang J (2008) Monodisperse hematite porous nanospheres: synthesis, characterization, and applications for gas sensors. *Nanotechnology* 19:125606–1256013
- [23] Brunauer S, Emmett PH, Teller E (1938) Adsorption of gases in multimolecular layers. *J Am Chem Soc* 60:309–319
- [24] Rouquerol F, Rouquerol J, Sing K (1999) *Adsorption by Powders & Solids*, Academic Press
- [25] Motaung DE, Makgwane PR, Ray SS (2015) Metal oxide nanostructures containing organic polymer hybrid solar cells: optimization of processing parameters on cell performance. *Appl Surf Sci* 355:484–494
- [26] Mishra YK, Modi G, Cretu V, Postica V, Lupan O, Reimer T, Paulowicz I, Hrkac V, Benecke W, Kienle L, Adelung R (2015) Direct growth of freestanding ZnO tetrapod networks for multifunctional applications in photocatalysis, UV photodetection and gas sensing. *ACS Appl Mater Interfaces* 7:14303–14316
- [27] Kicir N, Tüken T, Erken O, Gumus C, Ufuktepe Y (2016) Nanostructured ZnO films in forms of rod, plate and flower: electrodeposition mechanisms and characterization. *Appl Surf Sci* 377:191–199
- [28] Smith RDL, Prévot MS, Fagan RD, Zhang Z, Sedach PA, Siu MKJ, Trudel S, Berlinguette CP (2013) Photochemical route for accessing amorphous metal oxide materials for water oxidation catalysis. *Am Assoc Adv Sci* 340:60–63
- [29] David B, Pizúrová N, Synek P, Kudrle V, Jašek O, Schneeweiss O (2014)  $\epsilon$ -Fe<sub>2</sub>O<sub>3</sub> nanoparticles synthesized in atmospheric-pressure microwave torch. *Mater Lett* 116:370–373
- [30] Justus JS, Roy SDD, Raj AME (2016) Synthesis and characterization of hematite nanopowders. *Mater Res Express* 3:105037–1050315
- [31] Mohammadikish M (2014) Hydrothermal synthesis, characterization and optical properties of ellipsoid shape  $\alpha$ -Fe<sub>2</sub>O<sub>3</sub> nanocrystal. *Ceram Int* 40:1351–1358
- [32] Wang F, Qin XF, Meng YF, Guo ZL, Yang LX, Ming YF (2013) Hydrothermal synthesis and characterization of  $\alpha$ -Fe<sub>2</sub>O<sub>3</sub> nanoparticles. *Mat Sci Semicon Proc* 16:802–806
- [33] Montenegro DN, Hortelano V, Martínez O, Martínez-Tomas MC, Sallet V, Muñoz-Sanjósé V, Jimenez J (2013) Non-radiative recombination centres in catalyst-free ZnO nanorods grown by atmospheric-metal organic chemical vapour deposition. *J Phys D Appl Phys* 46:235302–235305
- [34] Calleja JM, Cardona M (1977) Resonant Raman scattering in ZnO. *Phys Rev B* 16:3753–3761

- [35] Özgür Ü, Alivov YI, Liu C, Teke A, Reshchikov MA, Dogan S, Avrutin V, Cho SJ, Morkoc H (2005) A comprehensive review of ZnO materials and devices. *J Appl Phys* 98:041301
- [36] Zhang R, Yin PG, Wang N, Guo L (2009) Photoluminescence and Raman scattering of ZnO nanorods. *Solid State Sci* 11:865–869
- [37] Sann J, Stehr J, Hofstaetter A, Hoffmann DM, Neumann A, Lerch M, Haboek U, Hoffmann A, Thomsen C (2007) Zn interstitial related donors in ammonia-treated ZnO powders. *Phys Rev B* 76:195203–195208
- [38] Shim SH, Duffy TS (2002) Raman spectroscopy of Fe<sub>2</sub>O<sub>3</sub> to 62 GPa. *Am Mineral* 87:318–326
- [39] Li J, Zhang H, Wang W, Qian Y, Li Z (2016) Improved performance of dye-sensitized solar cell based on TiO<sub>2</sub> photoanode with FTO glass and film both treated by TiCl<sub>4</sub>. *Phys B* 500:48–52
- [40] Wang P, Zhang X, Gao S, Cheng X, Sui L, Xu Y, Zhao X, Zhao H, Huo L (2017) Superior acetone sensor based on single-crystalline  $\alpha$ -Fe<sub>2</sub>O<sub>3</sub> mesoporous nanospheres via [C12mim][BF<sub>4</sub>]-assistant synthesis. *Sens Actuators B Chem* 241:967–977
- [41] Kubelka P, Munk F (1931) An article on optics of paint layers. *Fuer Tekn Physik* 12:593–609
- [42] Yi S, Zhao F, Yue X, Wang D, Lin Y (2015) Enhanced solar light-driven photocatalytic activity of BiOBr–ZnO heterojunctions with effective separation and transfer properties of photo-generated chargers. *New J Chem* 39:6659–6666
- [43] Etacheri V, Di Valentin C, Schneider J, Bahnemann D, Pillai SC (2015) Visible light activation of TiO<sub>2</sub> photocatalysts: advances in theory and experiments. *J Photochem Photobiol C* 25:1–29
- [44] Mamba G, Mishra A (2016) Advances in magnetically separable photocatalysts: smart, recyclable materials for water pollution mitigation. *Catalysts* 6:79–113
- [45] Lachheb H, Ajala F, Hamrouni A, Houas A, Parrino F, Palmisano L (2017) Electron transfer in ZnO–Fe<sub>2</sub>O<sub>3</sub> aqueous slurry systems and its effects on visible light photocatalytic activity. *Catal Sci Technol* 7:4041–4047
- [46] Studenikin SA, Golego N, Cocivera M, Fabrication of green and orange photoluminescent, undoped ZnO films using spray pyrolysis. *J Appl Phys* 84:2287–2294
- [47] Heo YW, Norton DP, Pearton SJ (2005) Origin of green luminescence in ZnO thin film grown by molecular-beam epitaxy. *J Appl Phys* 98:073502–073508
- [48] Usui H (2007) Influence of surfactant micells on morphology and photoluminescence of zinc oxide nanorods prepared by one-step chemical synthesis in aqueous solution. *J Phys Chem C* 111:9060–9065
- [49] Roy N, Roy A (2015) Growth and temperature dependent photoluminescence characteristics of ZnO tetrapods. *Ceram Intl* 41:4154–4160
- [50] Chettah H, Abdi D (2013) Effect of the electrochemical technique on nanocrystalline ZnO electrodeposition, its structural, morphological and photoelectrochemical properties. *Thin Solid Films* 537:119–123
- [51] Bousslama W, Elhouichet H, Férid M (2017) Enhanced photocatalytic activity of Fe doped ZnO nanocrystals under sun light irradiation. *Optik* 134:88–98
- [52] Sivula K, LeFormal F, Grätzel M (2011) Solar water splitting: progress using hematite ( $\alpha$ -Fe<sub>2</sub>O<sub>3</sub>) photoelectrodes. *Chem Sus Chem* 4:432–449
- [53] da Trindade LG, Zanchet L, Trench AB, Souza JC, Carvalho MH, de Oliveira AJA, Pereira EC, Mazzo TM, Longo E (2018) Flower-like ZnO/ionic liquid composites: structure, morphology, and photocatalytic activity. *Ionics* 25:1–14

**Publisher's Note** Springer Nature remains neutral with regard to jurisdictional claims in published maps and institutional affiliations.